J. dynamic behavior mater. (2017) 3:412–425
DOI 10.1007/s40870-017-0122-6

Compressive and Tensile Stress–Strain Responses of Additively Manufactured (AM) 304L Stainless Steel at High Strain Rates

B. Song[1] · E. Nishida[1] · B. Sanborn[1] · M. Maguire[1] · D. Adams[1] · J. Carroll[1] · J. Wise[1] · B. Reedlunn[1] · J. Bishop[1] · T. Palmer[2]

Received: 25 April 2017 / Accepted: 16 June 2017 / Published online: 28 June 2017

Abstract Additively manufactured 304L stainless steel with different build orientations and post-manufacturing processes was dynamically characterized in compression and tension at various high strain rates (~500, 1500, and 3000 s^{-1}) using Kolsky bar techniques. Wrought 304L stainless steel with a similar chemical composition as the additively manufactured material was also characterized at the same strain rates. The AM material exhibited higher yield and flow stresses in compression when the specimen strain is smaller than 0.3. In dynamic tension, the AM material also possessed higher yield and flow stresses but lower elongations to failure than the wrought material at all the strain rates tested. Depending on post processing and anisotropy, the high-rate yield strength of the AM 304L material is increased by 20–35%, compared to the yield strength of the wrought material.

Keywords Kolsky (split Hopkinson) bar · Compression · Tension · High strain rate · Additive manufacturing

Introduction

Additive manufacturing (AM) is a versatile approach to building a product by incrementally adding layers or elements until a final shape is made. Welding, brazing, or even layup of composite laminate materials are all considered traditional AM processes where post-processing is usually required. In addition to these, a new generation of AM processes, commonly known as 3D printing, have been recently developed. The new processes are digitally controlled with computer-aided design (CAD) and require little or no post-processing. In addition, the new AM technologies enable rapid prototyping, quicker design modifications, reduction of raw materials, and rapid part replacements to be increasingly utilized in mass customization applications for automobile, aerospace and construction industries [1]. Different AM technologies have been developed for producing a variety of materials. For example, Sandia National Laboratories developed Laser Engineered Net Shaping (LENS®), a type of additive technology which utilizes metal and alloy powders and a laser to create structural components defined by CAD models [2, 3]. New higher power, LENS®-like, AM processes have been recently developed to create components at much higher deposition rates.

The relationships between AM processing, microstructures, and material properties need to be understood before additively manufactured components can be used in critical applications, which has recently been reviewed by Frazier [4] and Herzog et al. [5]. AM processes often produce complex microstructures that vary spatially, resulting in non-uniform mechanical properties [6–9]. Furthermore, AM processing can often induce residual stresses [10] that alter a component's mechanical response. With respect to mechanical behavior, mechanical strength and ductility associated with damage initiation and evolution are critical for AM material applicability [11–13]. For example, Bian et al. [11] applied direct laser deposition technology to additively manufacture Ti–6Al–4V via fed powder and in situ laser delivery. The laser power, traverse speed, and powder feed rate produced non-uniform/transient thermal gradients and phase transformations during processing,

✉ B. Song
bsong@sandia.gov

[1] Sandia National Laboratories, 1515 Eubank Blvd. SE, Albuquerque, NM 87185, USA

[2] Pennsylvania State University, University Park, PA 16802, USA

resulting in a significant residual stress in the AM material. The AM Ti–6Al–4V alloy exhibited similar, or even superior, yield and ultimate tensile strength, but less ductility than those of the wrought material. Anisotropic mechanical behavior was also observed in the AM material [11]. Lu et al. [14] and Xu et al. [15] used powder bed fusion to additively manufacture Ti–6Al–4V alloys. Lu et al. [14] found that the AM Ti–6Al–4V produced by selective electron beam melting exhibited spatially varying microstructures, because the cooling rate varied from the bottom layer to the top layer. The inhomogeneous structures resulted in inconsistent tensile properties of the AM material. However, hot isostatic pressing (HIP) after AM homogenized the microstructures and led to highly consistent tensile properties. Xu et al. [15] tuned the variables such as energy density and focal offset distance in the selective laser melting process to optimize the microstructures in the AM Ti–6Al–4V alloy. They achieved similar tensile elongation and superior yield strength to the wrought material.

Almost all mechanical testing of AM material has involved quasi-static methods and only a few studies have dynamically characterized AM materials. Understanding the dynamic response of AM materials is critical for impact or shock applications, particularly if AM materials are substituted for conventional wrought materials. Li et al. [16] investigated the mechanical response of direct laser deposited Ti–6Al–4V alloy over a wide range of strain rates and temperatures. The compressive flow stress of the AM Ti–6Al–4V increased with increasing strain rates, yet the tensile flow stress decreased with increasing strain rates. Interestingly, the flow stress increased with increasing temperature, under both compressive and tensile loading conditions. It is even more intriguing that both yield strength and ultimate strength of the direct laser deposited Ti–6Al–4V alloy were found to be lower than for the conventional material made through forging processes. Fadida et al. [13] characterized the dynamic compressive behavior of Ti–6Al–4V additively manufactured through a direct laser deposited process. They found the direct laser deposited Ti–6Al–4V exhibited superior strength in both quasi-static and dynamic tests but comparable ductility to the same conventional material. Rodriguez et al. [17] investigated the quasi-static and dynamic tensile behaviors, as well as the strain-rate sensitivity, of electron beam additively manufactured Ti–6Al–4V. A distinct strain-rate effect was observed on strain hardening, thermal softening, and elongation of the additively manufactured alloy. Mohammadhosseini et al. [18] characterized strain-rate effect on the compressive behavior of Ti–6Al–4V alloy manufactured with electron beam melting method. The results showed that the additively manufactured Ti–6Al–4V alloy at dynamic strain rates exhibited a higher strength but less ductility than that at quasi-static strain rates.

AM stainless steels have also been dynamically characterized. Gray et al. [19] compared the constitutive and spallation response of LENS® manufactured 316L stainless steel to that of annealed wrought material and AM-as-built 316L stainless steel without recrystallization. Their preliminary results showed that the AM-as-built 316L stainless steel was approximately 60% higher in yield strength and 10% higher in spall strength than the annealed wrought material. The recrystallized AM 316L stainless steel exhibited similar quasi-static constitutive stress–strain response to the annealed wrought material but different spall response in terms of damage evolution. Nishida et al. [20] used Kolsky compression bar techniques to characterize wrought and LENS®-like additively manufactured 304L stainless steels. LENS® typically uses 500 W–1 kW laser powers with a focused beam, while the LENS®-like process used a 3.8 kW laser power and a defocused beam. In compression, the LENS®-like AM 304L stainless steel showed a higher yield strength but milder work hardening behavior than wrought 304L stainless steel at high strain rates. Within the dynamic strain rate range investigated in that study, the LENS®-like AM 304L stainless steel exhibited less strain-rate sensitivity in dynamic compressive response than the wrought material. Wise et al. [21] characterized the shock Hugoniot response of the same wrought and LENS®-like AM 304L stainless steels, and the AM material exhibited equal or greater dynamic strength. Recently, Inconel 625, boron carbide, and tungsten copper pseudoalloy have also been additively manufactured and dynamically characterized, respectively [22–25].

In this study, we employed pulse-shaped Kolsky compression and tension bar techniques to characterize the dynamic mechanical behavior of wrought and AM 304L stainless steels. The approach was similar to that in [20], but several differences exist.

1. Although both studies characterized the same wrought material, the AM stainless steel used herein was fabricated with a 2.0 kW LENS®-like process instead of a 3.8 kW LENS®-like process.
2. The 2.0 kW AM stainless steel was tested in the as-deposited condition and an annealed condition in both dynamic compression and tension, while [20] focused exclusively on the as-deposited condition in compression only.
3. Microstructural characterization was performed on the undeformed materials.

Materials and Specimens

Two forms of 304L stainless steel were tested in this study: wrought, ingot-derived material and 304L stainless steel

made by a laser-based additive process. Both forms consist of austenite with 1–3% ferrite (or martensite) by volume as determined by Feritscope and diffraction based measurements. The AM 304L stainless steel had a similar chemical composition as the wrought material used in baseline tests, but small differences were detected (see Appendix).

The AM 304L stainless steel was deposited using a process developed at Pennsylvania State University that directs a 2.0 kW laser beam onto a workpiece that is moved according to a crosshatch process. As shown in Fig. 1, the laser beam was aligned with the Z direction, while the crosshatches were aligned with the X and Y directions. Two sets of AM bars were built: X-bars and Z-bars. The lengths of the X-bars were aligned with the X direction, and the lengths of the Z-bars were aligned with the Z direction.

The Z bar is depicted on the left and the X bar on right. Dimensions were approximately $2.5 \times 2.5 \times 10$ cm.

In order to address the effect of residual stress during AM, two approaches have been conducted in this study. First, the specimens were extracted from central and edge locations in the as-deposited AM Z bars, as illustrated in the photograph in Fig. 2. Second, a separate annealing post processing was applied to the AM X-bars. Ideally, annealed X-bars (or Z-bars) would have been compared to as-deposited X-bars (or Z-bars), but sample quantities were limited. The annealing involved a 1 h heat treatment at 750 °C, and the effects were assessed with hardness tests, feritscope and optical microscopic measurements. As shown in Fig. 2, the Rockwell B hardness was measured before and after annealing along the edges of cylindrical blanks near the outer surface or near the center of a bar. A flat 6 mm wide surface was ground onto each cylindrical blank in order to make the measurement. The recovery anneal reduced the difference in hardness between the center and edge of the deposits. Higher hardness values remained near the baseplate interface, but all Kolsky bar samples were extracted at least 12.7 mm away from the baseplate. Feritscope measurements before and after annealing revealed a decrease from roughly 3% ferrite to 2% ferrite by volume. Finally, optical microscopy found cellular dendritic microstructures before and after annealing with only a slight amount of long-range diffusion after annealing.

Table 1 summarizes the detailed information of material processing and testing conditions. Measurements showed that the produced AM steel has an average density of 7832.6 kg/m^3 which is 99.4% that of the average value measured for the wrought steel. Additionally, no lack-of-fusion defects near build interfaces were found upon sectioning.

Wrought stainless steel 304L samples were extracted from a 10.1 cm-diameter, cold-finished cylindrical bar and characterized in compression and tension, along longitudinal and transverse directions, in order to compare the dynamic response between the AM material to the wrought

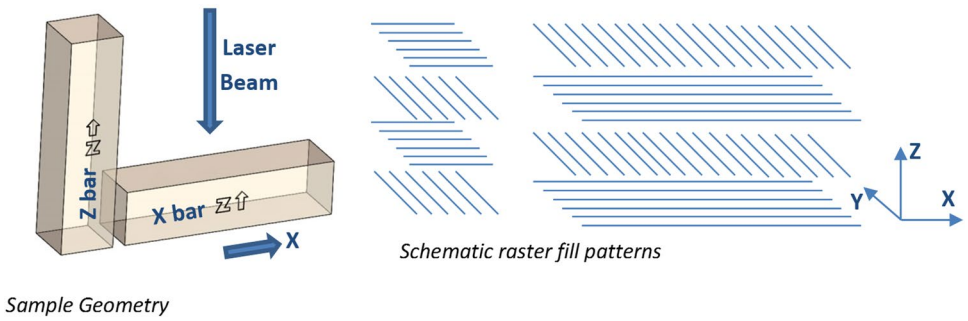

Fig. 1 Schematic of orientations of the additively manufactured 304L stainless steel bars

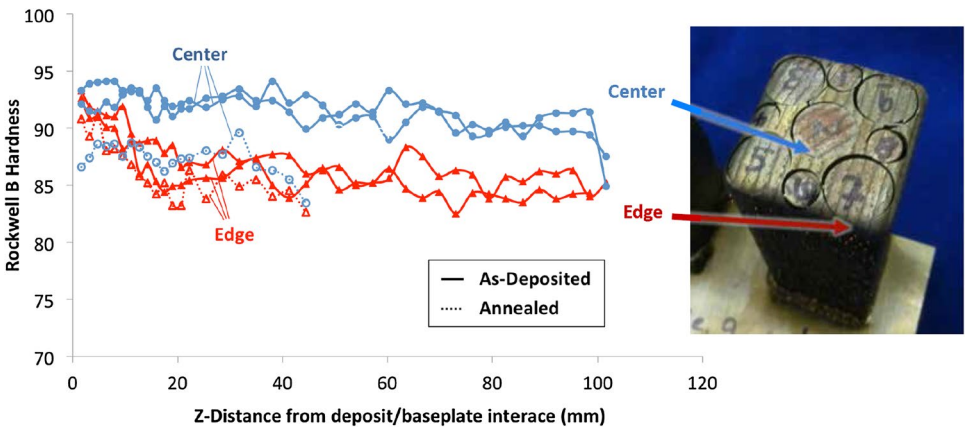

Fig. 2 Hardness along cylindrical blanks before and after a 1 h, 750 °C anneal

Table 1 Material processing information and testing conditions

Material	Orientation of test sample load axis	Post-processing	Strain rate (s^{-1})		Specimen location within parent bar
AM 304L; 2.0 kW Cross-hatched	X	Annealed	Compression	~500	Center
				~1500	Center
				~3000	Center
			Tension	~3000	Center
	Z	None (as-deposited)	Compression	~500	Center
				~500	Edge
				~1500	Center
				~1500	Edge
				~3000	Center
				~3000	Edge
			Tension	~3000	Center
				~3000	Edge
Wrought 304L	Longitudinal	None	Compression	~500	N/A
				~1500	N/A
				~3000	N/A
			Tension	~3000	N/A
	Transverse	None	Compression	~500	N/A
				~1500	N/A
				~3000	N/A
			Tension	~3000	N/A

material. A longitudinal test sample was machined with its loading axis aligned with the cylindrical billet axis. A transverse test sample was made with a loading axis aligned perpendicular to the billlet axis. Similarly, a transverse face is oriented perpendicular to the original cylinder axis.

Figure 3 shows a comparison of microstructures of wrought and 2.0 kW AM 304L stainless steels. Figure 3a–c includes several views of a transverse face of a wrought 304L stainless steel sample. The electron backscatter diffraction (EBSD) maps shown in Fig. 3a, b reveal a fine equiaxed grain structure in the wrought material. The colors indicate the crystallographic orientations of austenite grains with respect to the horizontal direction in the images (or left-to-right). The horizontal direction in Fig. 3a–c corresponds to the cylindrical billet axis (the longitudinal direction). As suggested in Fig. 3, the wrought material possesses an average austenite grain size of 28 μm. For the purposes of this paper, grain size is defined as the equivalent circle diameter at which grains larger than this amount comprise 50% of the EBSD map area. By this metric, using two different perpendicular sections for each material, the grain size of the AM crosshatch material is 141 μm. This metric is used because the AM materials contain wide distributions of grain sizes. As such, standard techniques similar to the linescan method (ASTM E112) and the EBSD area method (ASTM E2627) produce grain sizes (14 microns for wrought and 37 microns for AM crosshatch) that are considerably lower than typical grains observed (see Fig. 3). The scanning electron micrograph (SEM) shown in Fig. 3c shows a higher magnification view of microstructure with ferrite observed as long stringers and indicated with red arrows. The amount of ferrite suggested by these polished faces is consistent with the amount determined by X-ray diffraction (XRD) and Ferritscope. The microstructure maps and SEM image suggest that the wrought material is fully dense. There is no evidence of voids in the wrought material. Figure 3d shows a large area view of microstructure within a 2.0 kW, crosshatched AM 304L X bar stainless steel. The sample was moved such that the laser-induced melt pool travelled into the page (X) for one layer followed by movement left-to-right (in Y) with this process repeating until the end of a build. The map height in this figure is several mms. Thus, with a layer thickness ~0.89 mm, a portion of several layers is revealed within this map. This EBSD map shown in Fig. 3d demonstrates that the AM sample was nearly all austenite—consistent with XRD and Feritscope. Ferrite appears black in the EBSD maps in Fig. 3d, e but is finely distributed as opposed to the long stringers in the wrought material. In addition, the EBSD map shows no lack-of-fusion defects, large voids or other defects near layer interfaces. It is apparent from Fig. 3d that grains within the AM sample orient epitaxially from one layer to the next. Grains are larger than the wrought material (Fig. 3a) and those reported for

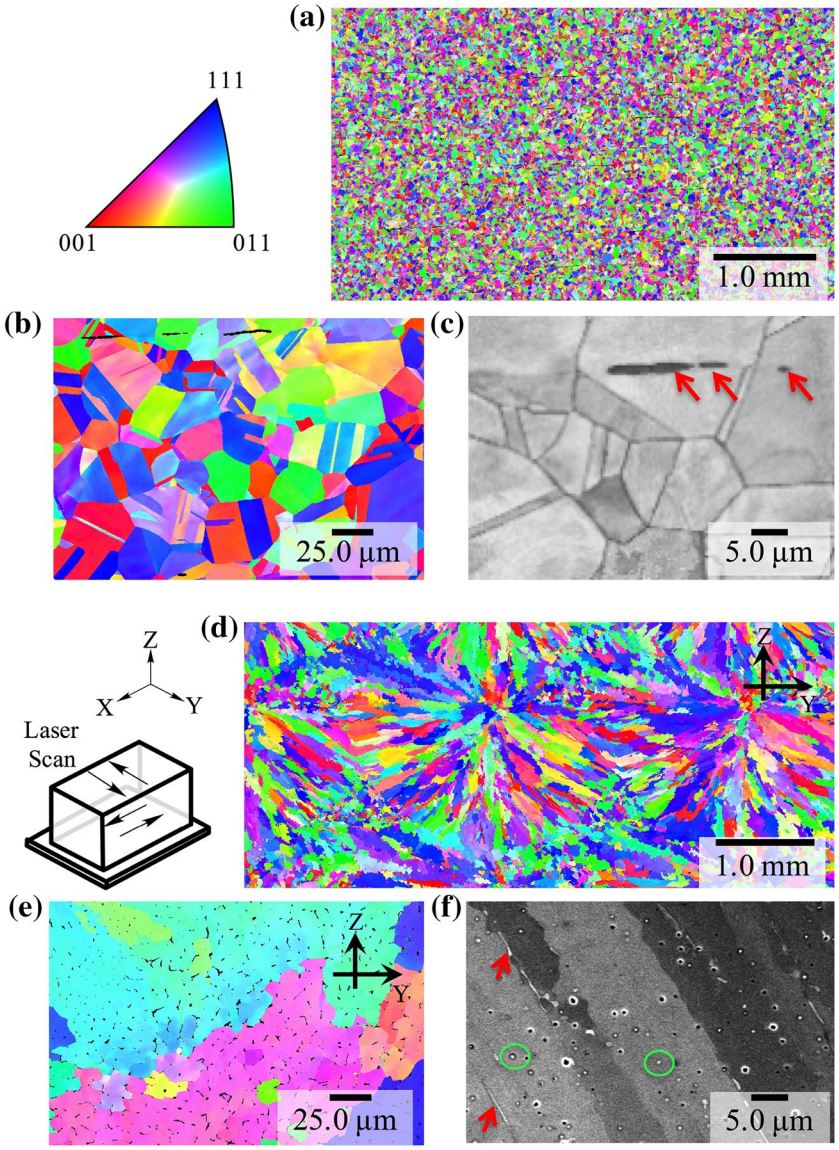

Fig. 3 Comparison of microstructures of (**a–c**) wrought and (**d–f**) AM 304L stainless steel samples. Austenite grains are *colored* according to their orientation, while ferrite appears *black* in EBSD maps (**a, b, d, e**). The ferrite is identified with red arrows in the SEM images (**c, f**). Oxide inclusions in the AM material are highlighted with *green circles*. (Color figure online)

traditional (low power) LENS® processes [3]. Finally, the AM steel has substantial sub-grain structure (Fig. 3e, f), which indicates a high dislocation density.

Both AM and wrought 304L stainless steels were machined with electric discharge machining (EDM) into two different specimen geometries. The compression specimens were cylindrical with a diameter of 6.35 mm and a height of $L_s = 3.18$ mm. The tensile specimens were made into a cylindrical dog bone shape with a 3.18 mm gage diameter and a $L_s = 6.35$ mm gage length. Figure 4 shows the schematic drawings for both compression and tensile specimens. Each compression specimen was sandwiched between the incident and transmission bars for dynamic compression tests. The tensile samples were directly threaded into the ends of the incident and transmission bars for dynamic tensile tests.

Dynamic Experiments

Dynamic compressive and tensile experiments were performed with Kolsky compression and tension bars, respectively.

Figure 5 shows a schematic of the Kolsky compression bar apparatus. In this study, the Kolsky compression bar system was made of Maraging C350 steel and had a common diameter of 19.05 mm. The incident and transmission bars were 3.66, and 1.83 m long, respectively. The striker was launched with a gas gun to impact the incident bar, generating a compressive stress wave (incident wave) propagating in the incident bar until it arrived at the specimen. Due to the lower mechanical impedance of the specimen than the pressure bars, part of the incident wave was reflected back into the incident bar and the rest transmitted

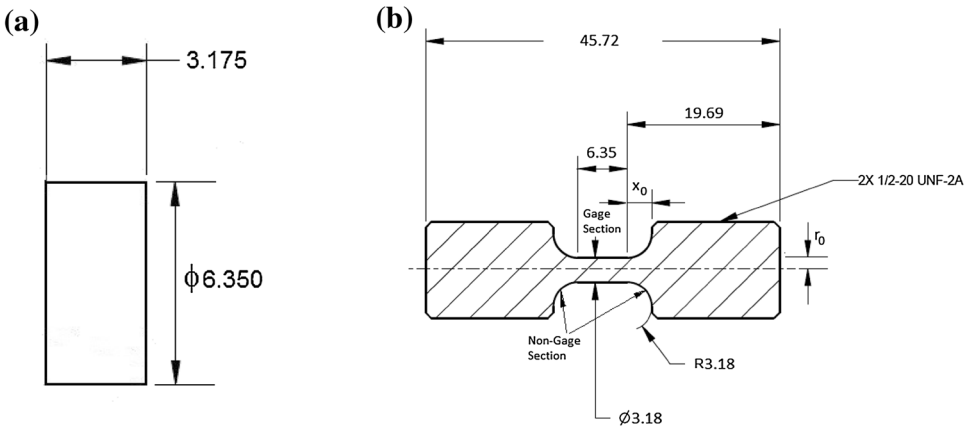

Fig. 4 Specimen designs for Kolsky bar experiments in (**a**) compression; and (**b**) tension. (Unit: mm except for the thread size in inch)

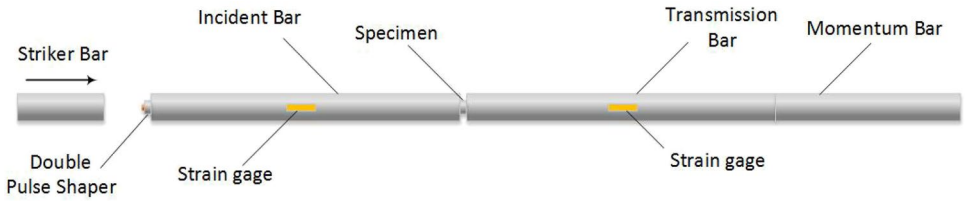

Fig. 5 Schematic of Kolsky compression bar

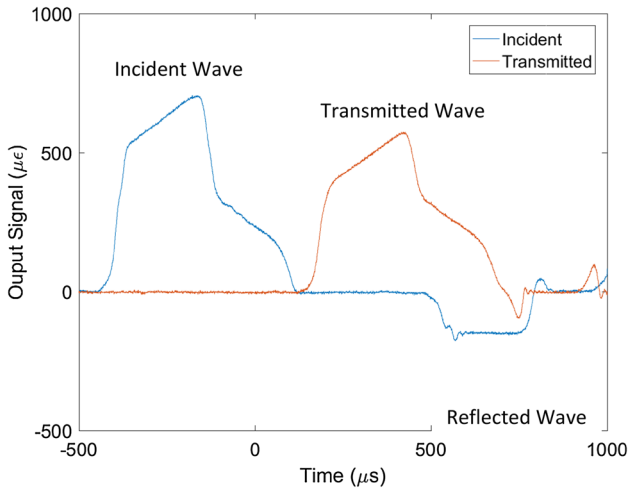

Fig. 6 A typical set of incident, reflected, and transmitted signals in a dynamic compression test

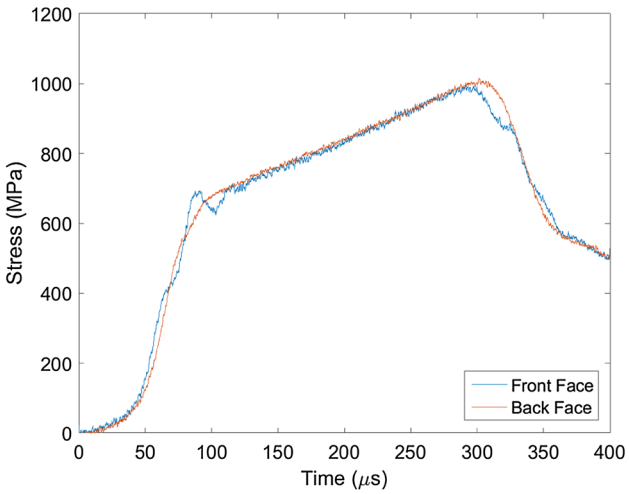

Fig. 7 Dynamic compressive stress equilibrium

through the specimen and into the transmission bar. As illustrated in Fig. 5, a double pulse shaping technique [26], where an annealed C11000 copper disk was stacked on a larger-diameter work-hardened steel disk on the impact end of the incident bar, was applied to generate a desired shape of incident pulse to achieve early dynamic stress equilibrium and nearly constant strain-rate deformation in a 304L stainless steel specimen.

Figure 6 shows a typical time history of the incident, reflected, and transmitted signals measured by the strain gages on the incident and transmission bars. These signals were generated in a double-pulse-shaped Kolsky compression bar test of a 2.0 kW, cross hatched, as-deposited AM 304L stainless steel material along Z direction. Through utilization of the double pulse shaping technique, the incident pulse was generated as a typical initial elasticity followed by a work hardening behavior, which is similar to the transmitted pulse, leading to a reflected pulse with a plateau. Figure 7 shows a comparison of engineering stresses at both ends of the specimen. The stress at the front face σ_1 and the stress at the back face σ_2 were calculated with the following respective equations,

$$\sigma_1 = \frac{A_0}{A_s} E_0 \left(\varepsilon_i + \varepsilon_r\right) \tag{1}$$

$$\sigma_2 = \frac{A_0}{A_s} E_0 \varepsilon_t \tag{2}$$

where ε_i, ε_r, and ε_t are incident, reflected, and transmitted bar engineering strains, respectively; E_0 is Young's modulus of the incident/transmission bar material; A_0 and A_s are cross-sectional areas of the bars and the specimen, respectively. The nearly overlapped stress histories at both ends of the specimen (Fig. 7) indicate that the specimen was equilibrated in stress over the nearly entire duration of dynamic compressive loading. The specimen stress can thus be calculated with either Eq. (1) or Eq. (2). Then the engineering strain rate and engineering strain in the specimen are calculated as,

$$\dot{\varepsilon} = -\frac{2C_0}{L_s} \varepsilon_r \tag{3}$$

$$\varepsilon = -\frac{2C_0}{L_s} \int_0^t \varepsilon_r dt \tag{4}$$

where C_0 is the elastic stress wave speed in the bar material; L_s is the gage length of the specimen. Equation (3) indicates that a plateau in the reflected pulse (Fig. 6) represents a constant strain rate in the specimen, due to the utilization of an appropriate double pulse shaping technique.

Figure 8 shows typical stress and strain histories in the specimen calculated with Eqs. (2) and (4), which were used to calculate stress–strain response by eliminating the term of time. In addition, the linear strain history in the specimen indicates a constant strain rate of roughly 500 s^{-1}.

Elastic indentation is known to significantly affect the stress–strain response measurement at small strains, i.e., Young's modulus, in a Kolsky compression bar test [27]. When the specimen is dynamically loaded in compression by the pressure bars, the smaller specimen may elastically indent the ends of the incident and transmission bars. This elastic indentation makes the stress wave at the bar/specimen interface no longer planar, which causes the conventional data reduction process [Eq. (4)] to overestimate the specimen strain. The overestimated specimen strain results in an underestimated Young's modulus of the specimen material. The pulse shaping technique minimizes stress wave dispersion and ensures early dynamic stress equilibrium, but does not correct the elastic indentation. Most recent research indicates that a combination of a pulse-shaped experiment and a numerical indentation correction significantly increases the accuracy of Kolsky compression bar experiments on small-strain compressive stress–strain response [28]. In this study, the indentation correction method developed by Safa and Gary [27] was applied to correct the indentation effect on the compressive stress–strain response of the 304L stainless steel.

The Kolsky tension bar system used in this study was made of Maraging C300 steel. The 25.4-mm-diameter incident and transmission bars were 3.62 and 2.13 m long, respectively. As shown in Fig. 9, a striker was launched to impact the end cap of the gun barrel, generating a tensile stress wave in the gun barrel. The tensile stress then transmits from the gun barrel into the incident bar via a coupler. Similar to the Kolsky compression bar test, a small annealed C11000 copper disk was placed on the end cap to generate a specific incident pulse to achieve stress equilibrium and constant strain rate deformation in the specimen. However, differing from the Kolsky compression bar test, the tensile specimens were threaded into the bar ends, which generated numerous interfaces that disturbed the stress wave propagation. In this study, we followed previous Kolsky tension bar experimental procedures:

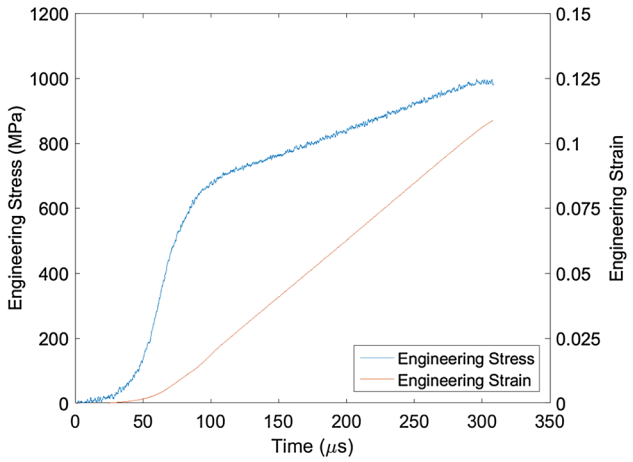

Fig. 8 Engineering compressive stress and strain histories in the specimen

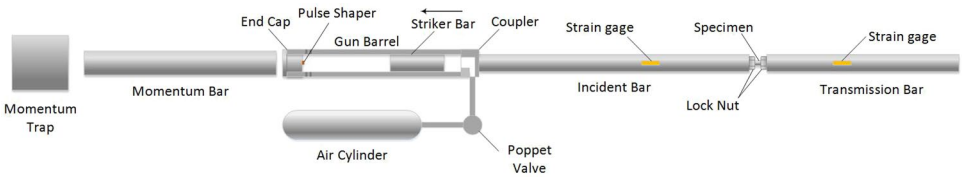

Fig. 9 A schematic of the Kolsky tension bar

1. Lock nuts were applied to the specimen to minimize the pseudo stress peak in the resultant stress–strain response [29].
2. A custom-made laser extensometer directly measured the displacement across the specimen free length, from one lock nut to the other lock nut [30].
3. The displacement over the tensile specimen gage section was deduced from the laser extensometer measurements using a numerical correction discussed briefly in the following paragraph.

Figure 10 shows a typical strain gage and laser extensometer time histories obtained from a Kolsky tension bar test of a wrought material along the longitudinal direction. It is seen that the displacement of the transmission bar end is much smaller than that of the incident bar end, which means the specimen was significantly elongated. The tensile stress history was calculated with the same equation [Eq. (2)]; whereas the strain history was calculated with the laser measurements by using the following equation [31, 32],

$$\varepsilon = \begin{cases} c' \frac{\delta}{L_s} & (\sigma \leqslant \sigma_y) \\ \frac{\delta - (1-c')\delta_y}{L_s} & (\sigma > \sigma_y) \end{cases} \quad (5)$$

where δ is the relative displacement across the front and back ends of the specimen, as measured by the laser extensometer; δ_y is the relative displacement across the front and back ends of the specimen when the dynamic yield strength is reached; σ_y is the dynamic yield strength of the tested material; and c' is the correction factor for specimen strain calculation at gage section. According to the specific design of the tensile specimen shown in Fig. 4b, the correction factor, c', has been determined as 0.62 in this study [32]. Figure 11 shows the calculated stress and strain histories in the tensile specimen subjected to a dynamic tensile load. Similar to the compression test, the nearly linear strain rate in the specimen indicates a nearly constant strain rate of 2900 s^{-1} during dynamic tensile loading.

Experimental Results and Discussion

Following the same procedure, the AM 304L stainless steel and wrought material listed in Table 1 were dynamically characterized in compression and tension. Three different strain rates (500, 1500, and 3000 s^{-1}) were conducted in compression; whereas, dynamic tensile tests were performed only at the strain rate of ~3000 s^{-1}. At each loading condition, 3–5 experiments were repeated to verify consistency. The mean curve was calculated as the representative curve at each testing condition. Figure 12a, b show the example results of individual compressive and tensile tests at the same conditions as shown in Figs. 6 and 10, respectively. Both compressive and tensile experimental results show very good repeatability at the same testing condition.

Figure 13 shows the dynamic compressive stress–strain curves of wrought and AM/Z-direction 304L stainless steel at various strain rates. In this figure, the stress–strain curves are bracketed into two groups to distinguish the AM and wrought materials. In each bracket, strain rate was represented with colors. In the bracket of wrought materials, the stress–strain curves at the same strain rate were distinguished with and without symbols for transverse (thick lines) and longitudinal (thin lines) directions, respectively. As shown in Fig. 13, all compressive stress–strain curves exhibit very similar elastic–plastic characteristics with

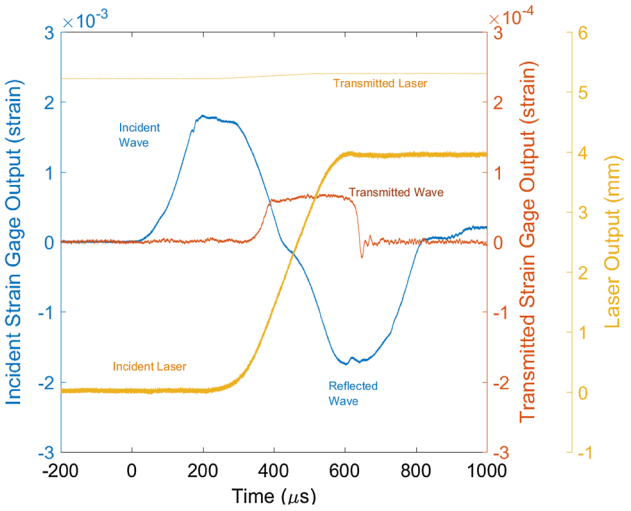

Fig. 10 A typical set of strain gage and laser extensometer signals from a Kolsky tension bar test

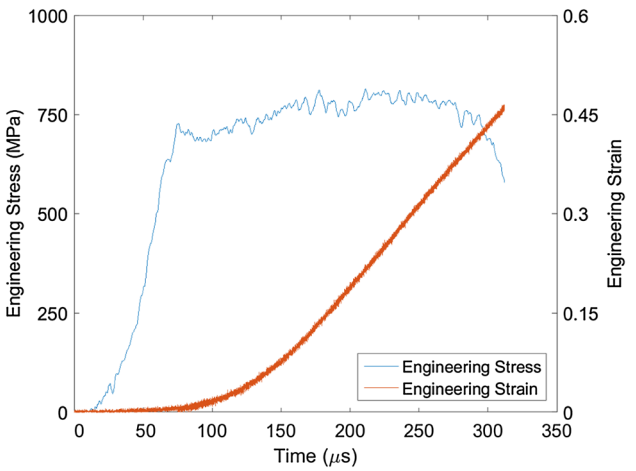

Fig. 11 Tensile stress and strain histories in the specimen

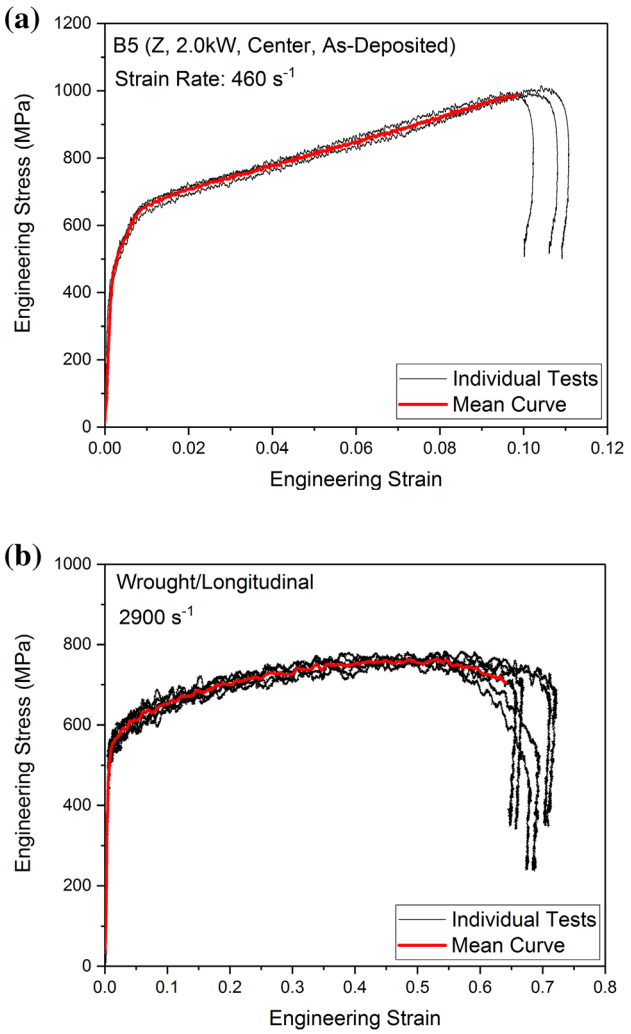

Fig. 12 Several engineering stress–strain curves of specimens at the same loading conditions and the corresponding mean curve. **a** Compressive stress–strain curves of AM material; **b** tensile stress–strain curves of wrought material at a higher strain rate

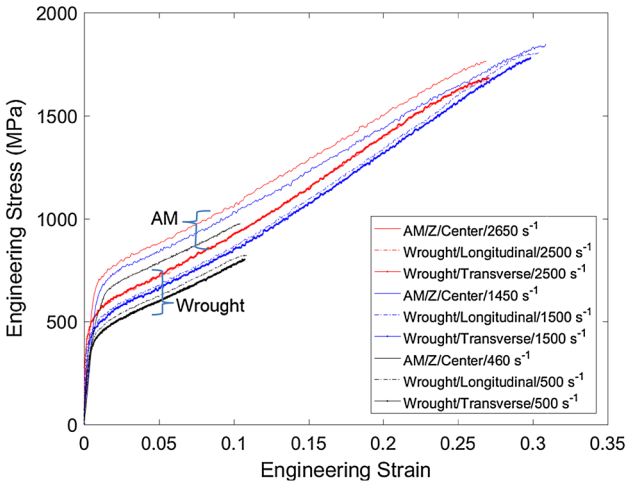

Fig. 13 Comparison of dynamic compressive stress–strain curves of wrought and AM/Z-direction 304L stainless steel

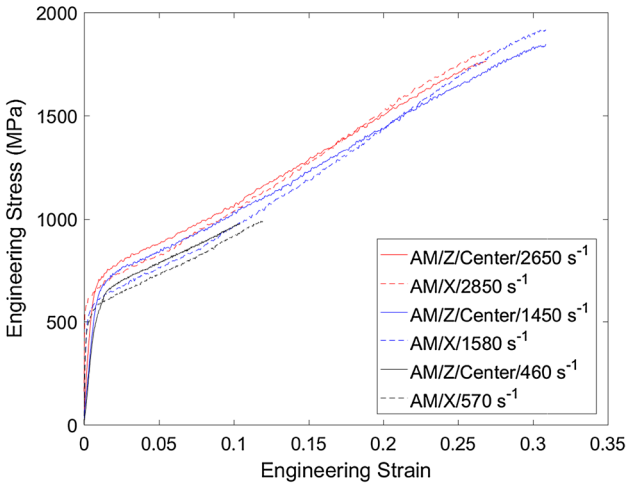

Fig. 14 Comparison of dynamic compressive stress–strain curves of AM 304L stainless steel along annealed X and as-deposited Z directions

significant sensitivities to strain rates. At similar strain rates, the wrought 304L stainless steel shows little difference in stress–strain response along the longitudinal and transverse directions. The AM/Z-direction 304L stainless steel exhibits higher yield and flow stresses by approximately 20% than the wrought material when the deformation is smaller than 30%. Due to limited loading duration, the specimens were compressed up to 30%. At the lowest dynamic strain rate (500 s^{-1}), the specimens were deformed to only 10%. However, one can still expect from Fig. 13 that the wrought 304L stainless steel possesses higher flow stress than the AM material at larger strains, showing a similar crossover feature between the wrought and AM stress–strain curves to that presented in [20]. The mechanism that caused the crossover is left for further research.

Figure 14 shows a comparison of dynamic compressive stress–strain curves of AM 304L stainless steel along X (annealed) and Z (as-deposited) directions. At each strain rate, the annealed samples along X direction exhibit a lower (less than 10%) yield and flow stress when specimen deformation is smaller than 0.2 than the as-deposited samples along Z direction. When specimen strain is larger than 0.2, the annealed X-direction samples had a higher flow stress than the as-deposited samples along Z direction. This indicates that the annealed X-direction samples had a higher work-hardening rate than the as-deposited Z-direction samples. However, it may be difficult to distinguish the effects of material orientation (X vs. Z direction) and post

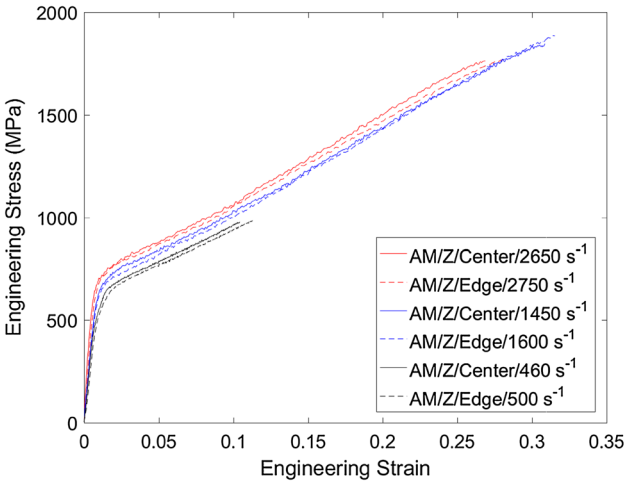

Fig. 15 Comparison of dynamic compressive stress–strain curves of AM 304L stainless steel along Z direction but at different locations

processing (as-deposited vs. annealing), which warrants additional tests in the future.

Figure 15 shows a comparison of dynamic compressive stress–strain curves of as-deposited AM/Z-direction samples from center and edge locations. At all three strain rates tested, the as-deposited AM/Z-direction stainless steel samples from the center of the parent bar had a little higher (less than 5%) flow stress than the samples from the edge of the parent bar.

The AM 304L stainless steel specimens show significantly different surface features from the wrought specimens after dynamic loading, as shown in Fig. 16, even though the shapes of the compressive stress–strain curves have only minor differences. The wrought stainless steel specimen still maintained a circular shape after dynamic compression (Fig. 16a). However, after dynamic compression, rough surfaces appear on both end and side of the AM specimen, clearly shown in Fig. 16b. This irregular surface morphology may be caused by significant

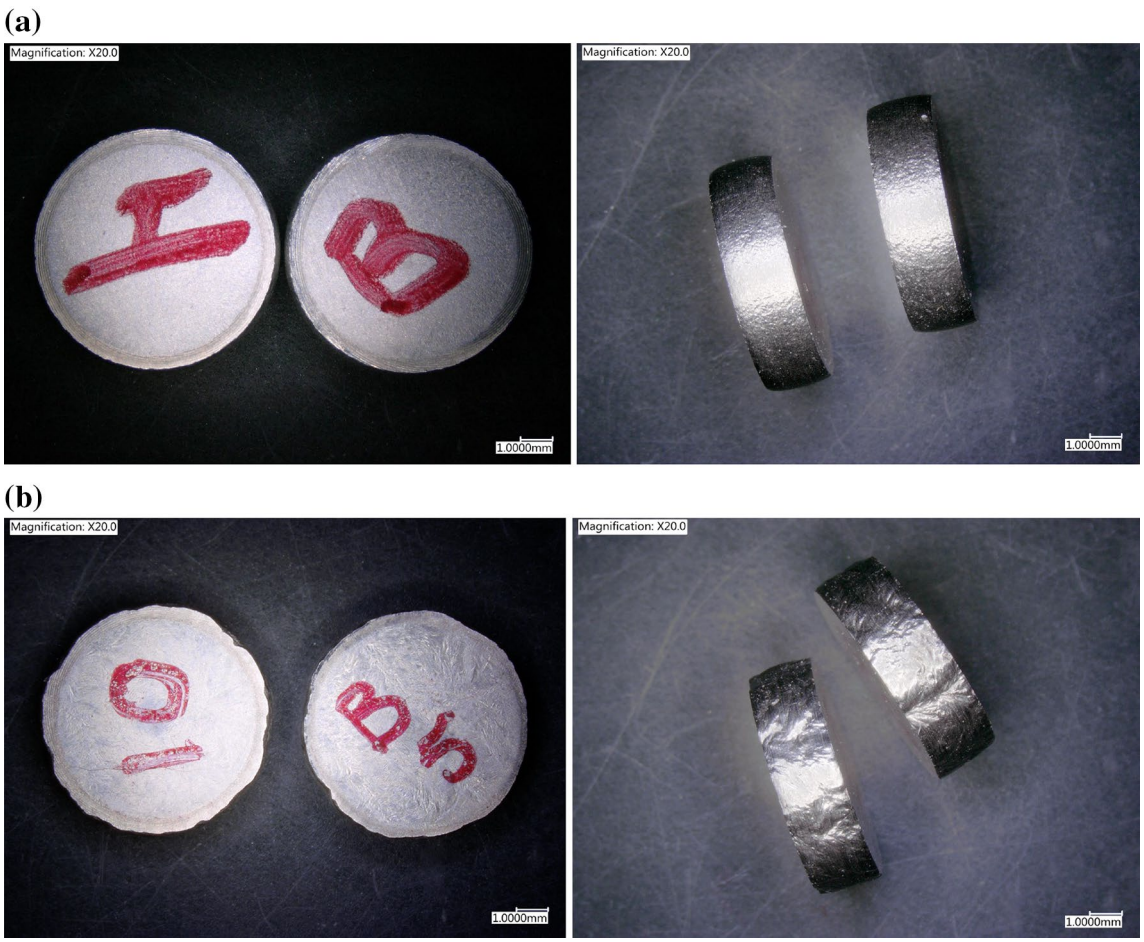

Fig. 16 Comparison of (**a**) wrought and (**b**) AM 304L stainless steel specimens after dynamic compression tests

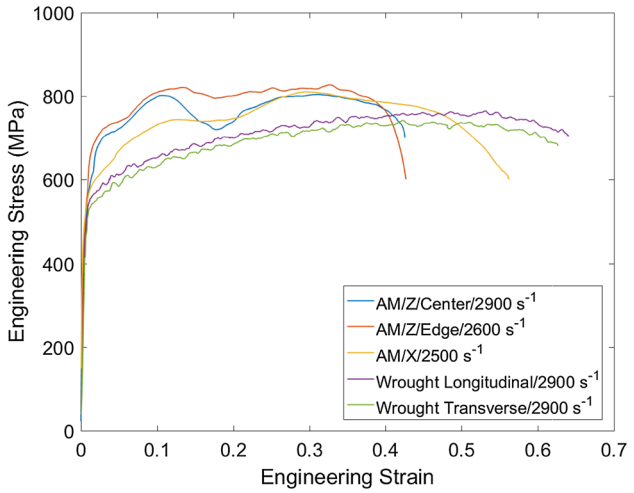

Fig. 17 Comparison of dynamic tensile stress–strain curves of wrought and AM 304L stainless steels at the strain rate of ~2900 s^{-1}

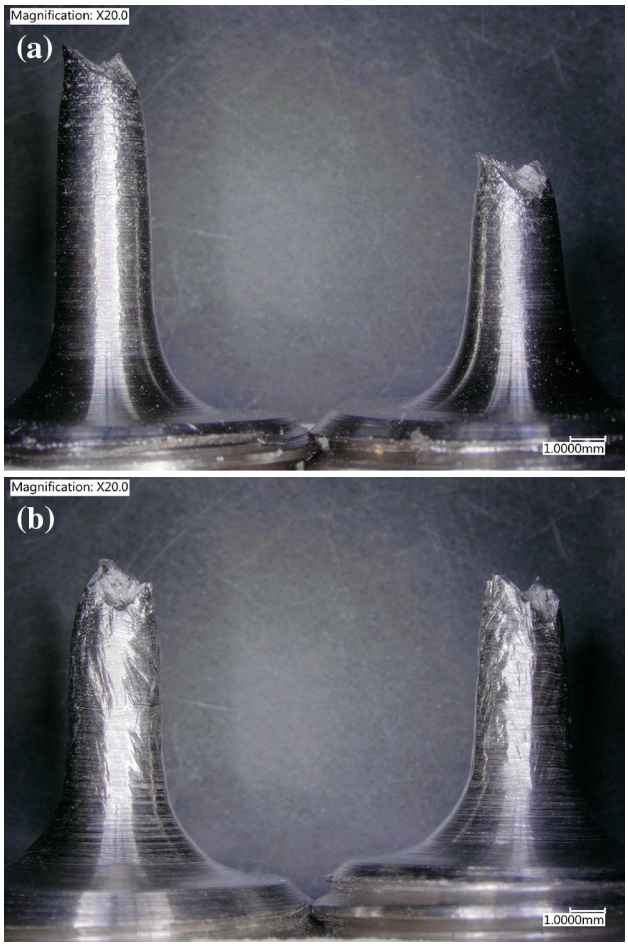

Fig. 18 Comparison of (**a**) wrought and (**b**) AM 304L stainless steel specimens after dynamic tensile tests

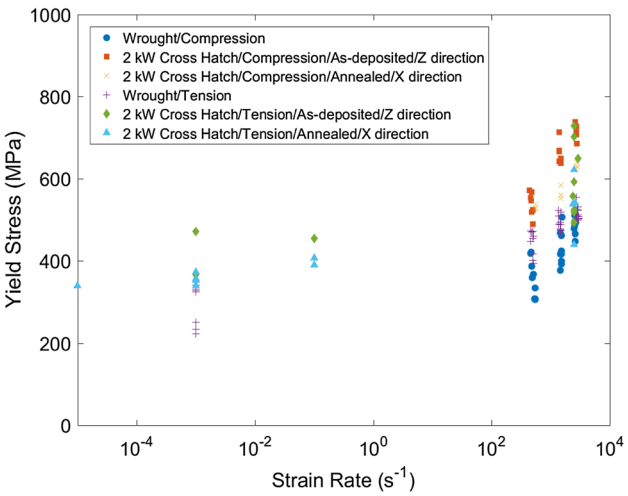

Fig. 19 Strain-rate effect on wrought and AM 304L stainless steels (the quasi-static data are from Ref. [33])

difference in microstructures, i.e., grain size, between the wrought and AM materials.

Figure 17 shows dynamic tensile stress–strain curves of wrought 304L stainless steel along longitudinal and transverse directions, and AM material at center and edge locations, at approximately the same strain rate of 2900 s^{-1}. The wrought material exhibits very similar stress–strain response along longitudinal and transverse directions. The flow stress along longitudinal direction is approximately 4% higher than along transverse direction for the wrought material. However, the tensile stress–strain response of the AM 304L stainless steel is quite different from that of wrought material. In general, the AM 304L stainless steel possesses higher flow stresses but lower elongation to failure than the wrought material. The flow stress in the AM material is approximately 15% higher than the wrought material but the elongation to failure decreases from 65% for the wrought material to 40% for the AM material. In addition, the flow stress in the AM material decreases when the strain is larger than 10% and then picks up at the strain of 17% (a "V-shape" shown in Fig. 17). This could be a result of the large grain sizes in the AM materials resulting in approximately 115 grains in each cross section of the specimen, but we believe it may indicate a microstructural change or slip mechanism in the material subjected to high-strain-rate tensile load. In-depth microstructural investigation is required to explain the mechanism, which has been planned and will be presented in the future. After dynamic tension tests, the failed AM 304L stainless steel specimens, as shown in Fig. 18b, showed very similar surface features to the compression specimens

shown in Fig. 16b. However, the surfaces of the wrought specimens were smooth after dynamic failure, also shown Fig. 18a.

In order to investigate strain rate effects, Fig. 19 shows the yield strengths of both wrought and AM 304L stainless steels at different strain rates varying from quasi-static [33] to dynamic strain rates. Both wrought and AM materials show a strong strain rate effect where yield strength significantly increases with increasing strain rate. The strain-rate sensitivity within the dynamic strain rate regime is significantly higher than that within the quasi-static strain rate regime for both wrought and AM materials. Even though the AM 304L stainless steel samples exhibit higher yield strengths than the wrought material, the dynamic strain-rate sensitivities for AM 304L stainless steels are similar to the wrought material. In addition, for the same material at the similar strain rate, i.e., ~2500 s^{-1}, both wrought and AM 304L materials showed a little higher yield stress in tension than in compression.

Conclusions

In this study, Kolsky compression and tension bar techniques have been applied to dynamically characterize the compressive and tensile stress–strain responses of additively manufactured 304L stainless steel with different orientations with respect to the AM processes. As a reference, wrought 304L stainless steel with similar chemical composition was also characterized at the same strain rates. The experimental results showed that the AM 304L stainless steel exhibited higher yield and flow stresses than the wrought material when the strain magnitude was less than 30%, in both compression and tension. For example, at a compressive strain rate of 2500 s^{-1} the yield and flow stresses were roughly 20% higher in the AM material. For compressive strains greater than 30%, the AM materials may possess lower flow stresses than the wrought material. In dynamic tension, the as-deposited AM material showed about 35% less elongation to failure than the wrought material. Both AM and wrought 304L stainless steel show significant, yet similar, strain-rate sensitivity for strain rate magnitudes above 500 s^{-1}.

Acknowledgements The authors appreciate the efforts of (A) Kilgo for sample preparation and (B) McKenzie for SEM and EBSD. Sandia National Laboratories is a multi-mission laboratory managed and operated by National Technology and Engineering Solutions of Sandia, LLC., a wholly owned subsidiary of Honeywell International, Inc., for the U.S. Department of Energy's National Nuclear Security Administration under contract DE-NA-0003525.

Appendix

This appendix presents the chemical compositions of AM and wrought materials (See Tables 2, 3).

Table 2 Measured composition of received powder and material deposited using $P_{avg} = 2.0$ kW (remainder as Fe)

Elemental constituent	Powder composition (wt%) from ICP-MS	Powder composition (wt%) from Leco[a]	Deposit composition (wt%) from Leco[a]	Deposit composition (wt%) from OES
C	n/m	0.015	0.010	n/m
Cr	19.07	n/m	n/m	19.02
Cu	0.03	n/m	n/m	0.03
Mn	1.55	n/m	n/m	1.48
Mo	0.04	n/m	n/m	0.04
N	n/m	0.089	0.081	n/m
Ni	10.38	n/m	n/m	9.97
O	n/m	0.017	0.023	n/m
P	0.006	n/m	n/m	0.012
S	0.006	0.006	0.008	n/m
Si	0.5	n/m	n/m	0.55
V	0.02	n/m	n/m	0.03

ICP inductively couple plasma, *MS* mass spectroscopy, *OES* optical emission spectroscopy

[a]Measurements by Leco involved gas fusion (for O, N) and combustion for (C, S)

Table 3 Elemental composition of cold finished wrought 304L bar (remainder as Fe)

Elemental constituent	Composition (wt%)
C	0.013
Cr	19.5
Cu	n/m
Mn	1.5
Mo	0.027
N	0.049
Ni	10.1
O	n/m
P	0.015
S	0.015
Si	0.58
V	0.02

References

1. WSTIAC (2014) Building the future, one layer at a time. AMMTIAC WSTIAC J 3:3–6
2. Atwood C, Griffith M, Harwell L, Schlienger E, Ensz M, Smugeresky J, Romero T, Greene D, Reckaway D (1998) Laser engineered net shaping (LENS™): a tool for direct fabrication of metal parts, Sandia report, SAND98-2473C. Sandia National Laboratories, Albuquerque
3. Gill DD, Smugeresky JE, Robino CV, Harris MF, Griffith ML (2004) On the interface between LENS® deposited stainless steel 304L repair geometry and cast or machined components, Sandia report, SAND2004-4035. Sandia National Laboratories, Albuquerque
4. Frazier WE (2014) Metal additive manufacturing: a review. J Mater Eng Perform 23:1917–1928
5. Herzog D, Seyda V, Wycisk E, Emmelmann C (2016) Additive manufacturing of metals. Acta Mater 117:371–392
6. Li J, Monaghan T, Masurtschak S, Rournias-Varotsis A, Friel TJ, Harris RA (2015) Exploring the mechanical strength of additively manufactured metal structures with embedded electrical materials. Mater Sci Eng A 639:474–481
7. Sharma VS, Singh S, Sachdeva A, Kumar P (2015) Influence of sintering parameters on dynamic mechanical properties of selective laser sintered parts. Int J Mater Form 8:157–166
8. Ladani L, Razmi J, Choudhury SF (2014) Mechanical anisotropy and strain rate dependency behavior of Ti6Al4V produced using E-beam additive fabrication, transactions of the ASME. J Eng Mater Technol 136(3):031006
9. Gu J, Ding J, Williams SW, Gu H, Bai J, Zhai Y, Ma P (2016) The strengthening effect of inter-layer cold working and post-deposition heat treatment on the additively manufactured AL-6.3Cu alloy. Mater Sci Eng A 651:18–26
10. Mooney J (2006) Stress relief of 304L stainless steel LENS Material, Federal Manufacturing & Technologies report, KCP-613-8193
11. Bian L, Thompson SM, Shamsaei N (2015) Mechanical properties and microstructural features of direct laser-deposited Ti–6Al–4V. JOM 67:629–638
12. Carlton HD, Haboub A, Gallegos GF, Parkinson DY, MacDowell AA (2016) Damage evolution and failure mechanisms in additively manufactured stainless steel. Mater Sci Eng A 651:406–414
13. Fadida R, Rittel D, Shirizly A (2015) Dynamic mechanical behavior of additively manufactured Ti6Al4V with controlled voids, transactions of the ASME. J Appl Mech 82:041004
14. Lu SL, Tang HP, Ning YP, Liu N, Stjohn DH, Qian M (2015) Microstructure and mechanical properties of long Ti–6Al–4V rods additively manufactured by selective electron beam melting out of a deep powder bed and the effect of subsequent hot isostatic pressing. Metall Mat Trans A 46A:3824–3834
15. Xu W, Sun S, Elambasseril J, Liu Q, Brandt M, Qian M (2015) Ti–6Al–4V additively manufactured by selective laser melting with superior mechanical properties. JOM 67:669–673
16. Li P-H, Guo W-G, Huang W-D, Su Y, Lin X, Yuan K-B (2015) Thermomechanical response of 3D laser-deposited Ti–6Al–4V alloy over a wide range of strain rates and temperatures. Mater Sci Eng A 647:34–42
17. Rodriguez OL, Allison PG, Whittington WR, Francis DK, Rivera OG, Chou K, Gong X, Butler TM, Burroughs JF (2015) Dynamic tensile behavior of electron beam additive manufactured Ti6Al4V. Mater Sci Eng A 641:323–327
18. Mohammadhosseini A, Masood SH, Fraser D, Jahedi M (2015) Dynamic compressive behaviour of Ti–6Al–4V alloy processed by electron beam melting under high strain rate loading. Adv Manuf 3:232–243
19. Gray GT III, Livescu V, Rigg PA, Trujillo CP, Cady CM, Chen SR, Carpenter JS, Lienert TJ, Fensin S (2015) Structure/property (constitutive and dynamic strength/damage) characterization of additively manufactured 316L SS. Eur Phys J 94:02006
20. Nishida E, Song B, Maguire M, Adams D, Carroll J, Wise J, Bishop J, Palmer T (2015) Dynamic compressive response of wrought and additive manufactured 304L stainless steels. Eur Phys J 94:01001
21. Wise JL, Adams DP, Nishida EE, Song B, Maguire MC, Carroll J, Reedlunn B, Bishop J, Plamer TA (2015) Comparative shock response of additively manufactured versus conventionally wrought 304L stainless steel. In: Proceedings of 19th Biennial APS conference on shock compression of condensed matter (SCCM15), AIP conference proceedings, Tampa, Florida, 14–19 June 2015
22. Puppala G, Moitra A, Sathyanarayanan S, Kaul R, Sasikala G, Prasad RC, Kukreja LM (2014) Evaluation of fracture toughness and impact toughness of laser rapid manufactured Inconel-625 structures and their co-relation. Mater Des 59:509–515
23. Rivera OG, Allison PG, Jordon JB, Rodriguez OL, Brewer LN, McClelland Z, Whittington WR, Francis D, Su J, Martens RL, Hardwick N (2017) Microstructures and mechanical behavior of Inconel 625 fabricated by solid-state additive manufacturing. Mater Sci Eng A 694:1–9
24. Hayun S, Paris V, Dariel MP, Frage N, Zaretzky E (2009) Static and dynamic mechanical properties of boron carbide processed by spark plasma sintering. J Eur Ceram Soc 29:3395–3400
25. Guo W, Liu J, Li S, Zhang H, Zhao Z, Cheng X (2014) The effect of preparation methods on the microstructure and dynamic compressive properties of 65W–25Cu–10Ni alloys. Int J Refract Metal Hard Mater 48:238–244
26. Frew DJ, Forrestal MJ, Chen W (2005) Pulse shaping techniques for testing elastic-plastic materials with a split Hopkinson pressure bar. Exp Mech 45:186–195
27. Safa K, Gary G (2010) Displacement correction for punching at a dynamically loaded bar end. Int J Impact Eng 37:371–384
28. Song B, Nishida E, Corona E (2015) Data-reduction uncertainties in Kolsky bar experiments on metals, 2015 SEM Annual conference & exposition on experimental & applied mechanics, Costa Mesa, California, USA, 8–11 June 2015
29. Song B, Antoun BR (2012) Pseudo stress response in Kolsky tension bar experiments. Exp Mech 52:525–528

30. Nie X, Song B, Loeffler CM (2015) A novel splitting-beam laser extensometer technique for Kolsky tension bar experiment. J Dyn Behav Mater 1:70–74
31. Song B, Antoun BR, Jin H (2013) Dynamic tensile characterization of a 4330-V steel with Kolsky bar techniques. Exp Mech 53:1519–1529.
32. Song B, Wakeland PE, Furnish M (2015) Dynamic tensile characterization of Vascomax® maraging C250 and C300 alloys. J Dyn Behav Mater 1:153–161
33. Adams DP, Reedlunn B, Maguire MC, Song B, Carroll J, Bishop JE, Wise JL, Kilgo A, Palmer TA, Brown DW, Clausen, B, Vogel SC (2016) Mechanical response of additively manufactured stainless steel 304L across a wide range of loading conditions, Sandia report, SAND2016-11859. Sandia National Laboratories, Albuquerque